A novel strategy for 2D/2D NiS/graphene heterostructures as efficient bifunctional electrocatalysts for overall water splitting

Deliang Zhang[a,1], Hongyu Mou[b,1], Fu Lu[b], Caixia Song[b,*], Debao Wang[a,*]

[a] Key Laboratory of Optic-electric Sensing and Analytical Chemistry for Life Science (MOE), and College of Chemistry and Molecular Engineering, Qingdao University of Science and Technology, Qingdao, 266042, PR China
[b] College of Materials Science and Engineering, Qingdao University of Science & Technology, Qingdao, 266042, PR China

ABSTRACT

Designing non-precious-metal bifunctional electrocatalysts with highly efficient overall water splitting in basic media still remain a signification challenge. In this work, an environment-friendly and one-step strategy is developed to synthesize two-dimensional (2D/2D) NiS/graphene heterostructure composites via a pyrolysis accompanied sulfidation process using novel deep eutectic solvents (DESs) as precursors. The as-obtained 2D NiS/graphene heterostructures manifest excellent HER and OER activity in alkaline solution. Furthermore, the optimized 2D/2D heterostructure as a bifunctional catalyst for overall water splitting exhibits a low cell voltage of 1.54 V at 10 mA cm^{-2} in alkaline media, even superior than that of the integrated Pt/C and IrO$_2$ couples. The one-step DESs based procedure favors the interface coupling between graphene and NiS nanosheets, which significantly brings high surface-active sites exposure, enhances electrical conductivity, and results in high electrocatalytic activity. The DESs precursor has the advantage of solution reaction and acts as an environment-friendly synthetic strategy for clean energy generation.

1. Introduction

Hydrogen (H$_2$) is considered to be the most promising clean energy carrier in the near future due to its renewable and environmental-friendly properties. Electrochemical or photoelectrochemical catalyzing water splitting is an environmentally friendly approach for providing affordable H$_2$ [1]. Generally, the scalable water splitting prefers to effective and stable non-noble metal electrocatalysts instead of the state-of-the-art noble-metal catalysts for hydrogen evolution reaction (HER) and oxygen evolution reaction (OER) [2,3]. Recently, 3d transition metals (TMs) such as Fe, Co, Ni, and their derivatives have received increasing attention as potential replacements of Pt-based catalysts owing to their earth abundance and low cost [4–6]. Their compounds, such as phosphides [7–9], sulfides [10,11], (hydro)oxides [12], and selenides [13], have been well studied as substitutes for Pt-based catalysts. Unfortunately, the inadequacy of the HER activity of transitional metal compounds is obvious comparing to Pt based catalysts, and the essence can attribute to the limited active site exposure and intrinsic low electrical conductivity. Moreover, most of the TMs based electrocatalytic water splitting only participates in one HER or OER semi-reaction, and few studies report it for the overall water splitting.

Through providing larger surface area or/and combining with other components, 2D heterostructure can provide more contact area and rich exposed active sites to achieve high-efficiency HER catalytic activity compared with the traditional nanomaterials with limited active sites. For instance, Boppella et al. reported 2D cobalt phosphide/nickel-cobalt phosphide heterostructure on N-doped carbon, which exhibited highly efficient HER performance [14]. Xu et al. demonstrated a nanoforest electrocatalyst with the self-assembly of ultrathin Ni(OH)$_2$/Ni$_3$S$_2$ nanosheets using a high-temperature and large-potential electrodeposition technique exhibiting excellent HER catalytic activity [15]. Xi's group reported a two-step process to synthesize FeS$_2$/CoS$_2$ nanosheets as efficient bifunctional electrocatalyst for overall water splitting [16]. Another effective strategy to improve the electrocatalytic activity is coupling the electrocatalyst on graphene or other carbon materials to enhance the electrical conductivity [17]. For example, Rout et al. proposed a solvothermal process to fabricate MoS$_2$ nanosheets on the surface of graphene. The obtained MoS$_2$/graphene nanohybrids exhibit superior HER electrocatalytic activity [18]. Therefore, through precise electronic structure regulation and active component integration, desirable water splitting electrocatalysts have been synthesized [19–21].

---

* Corresponding authors.
  E-mail addresses: songcaixia@qust.edu.cn (C. Song), dbwang@qust.edu.cn (D. Wang).
[1] These authors contribute equally to this work.

Nickel sulfide is a promising catalyst for water splitting due to its low cost, earth abundance, and environment-friendly [22]. However, nickel sulfide has poor stability and high overpotential in alkaline media, which greatly limits its electrocatalytic performance [23]. Combining nickel sulfide with graphene can effectively improve its electrocatalytic activity and durability. At present, many preparation methods have been reported for nickel sulfide/graphene (carbon) composite. For instance, Wu's group reported a three-step method to prepare carbon-encapsulated nickel sulfide core-shell architectures by pyrolysis of S-Ni(II)-containing polypyrrole solid precursors [24]. Qu et al. prepared graphene/nickel sulfide composites, which involved the preparation of graphene, dispersion of graphene in a solution of Ni-MOF, and then freeze-drying and pyrolysis [25]. Zou et al. prepared Ni_xS_y/graphene by a three-step procedure, including preparation of graphene oxide, preparation of NiO/graphene by chemical bath deposition, and preparation of Ni_xS_y/graphene by anion exchange [26]. These nickel sulfide/graphene preparation methods are more complex and usually involve waste water or other organic solvents discharging. Thus, it is an urgent need to develop a simple, cheap, and environment-friendly method to prepare nickel sulfide/graphene composites. In addition, surface energy mismatch makes it difficult for graphene to disperse in water or other organic solvents. Therefore, catalytic activity of the obtained graphene composites cannot be fully exhibited.

Recently, deep eutectic solvents (DESs) have been applied in many fields such as analytical chemistry, electrochemistry, chemical synthesis, material chemistry, and catalysis· based on the unique physicochemical properties such as tunable compositions, powerful solvation ability, less expensive, and environmentally friendly [27]. There are many works exploring the potential to use choline chloride based DESs as reaction media to synthesize zeolite-type materials, metal–organic frameworks, nano-metals, carbon materials, etc. [28]. To the best of our knowledge, no reports have concerned the synthesis of transition metal sulfides/graphene composites in the environment-friendly DESs media.

Herein, novel DESs of $NiCl_2 \cdot 6H_2O$/polyethylene glycol 200 (PEG 200) with different mole ratios were elaborately designed and were used as precursors to synthesize 2D NiS/graphene (NiS/G) heterostructure composites via a pyrolysis accompanied sulfidation process. The strategy shows several advantages. Firstly, the designed DESs is an environment-friendly homogeneous system which can make sufficient contact between components. Secondly, the growing and coupling of NiS and graphene take place in one-step, which can effectively make the composite materials uniformly coupled. In addition, the uniformly coupled graphene can effectively improve electrical conductivity and protect NiS nanosheets from corrosion. Moreover, the synthetic strategy can be extended to the preparation of other transition metal sulfide/graphene composites, providing new candidates for highly efficient electrocatalysts. Such 2D NiS/G heterostructure exhibits highly efficient OER and HER activities in 1 mol L^{-1} KOH solution. While utilized as a bifunctional electrocatalyst, it also shows highly efficient overall water splitting capability with a cell voltage of 1.54 V at 10 mA·cm^{-2} in alkaline electrolysis cell.

2. Experimental

2.1. Synthesis of the electrocatalysts

$NiCl_2 \cdot 6H_2O$ and polyethylene glycol 200 (PEG 200) were purchase from Macklin, sublimed sulfur were purchase from Sino pharm Chemical Reagent Co., Ltd, and all other chemical materials were purchase from Sigma-Aldrich without further purification.

The 2D NiS/graphene heterostructures were prepared by pyrolysis and sulfidation of a deep eutectic solvent (DES). In a typical procedure, $NiCl_2 \cdot 6H_2O$ (2.377 g) and PEG 200 (8 g) were mixed, heated with an oil bath at 50 °C, and stirred to form a uniform liquid (DES). The resulting DES liquid in a porcelain boat was put into the tube furnace together with sublimed sulfur at the upstream side, and then, was heated to 550

°C by programmed heating and held for 4 h under flowing nitrogen atmosphere. As the furnace cooled, the 2D NiS/graphene heterostructures were obtained. For comparison, the NiS/graphene 2D heterostructures with different loading amount of graphene were synthesized following the same procedure by changing the amount of PEG 200 used. The amount of $NiCl_2 \cdot 6H_2O$ was 2.377 g and PEG 200 in the experiment were 4.0 g, 6.0 g, 8.0 g, and 10.0 g forming DES-1, DES-2, DES-3, and DES-4, which were used as precursors for the preparation of catalysts NiS/G-1, NiS/G-2, NiS/G-3, and NiS/G-4, respectively.

2.2. Characterization

To identify the formation of DESs, solution ^{1}H NMR experiments were performed on a Bruker DMX 300 NMR spectrometer (300 MHz) with d6-dimethyl sulfoxide as the standard. The chemical shift data were later processed by the MestReNova Program. Differential scanning calorimetry (DSC) was performed using a Q2000 DSC (TA Instruments-Waters LLC, USA) system at a heating rate of 10 °C min^{-1}.

The powder X-ray diffraction (XRD) patterns were collected using a D/max-2500/PC X-ray diffractometer using Cu Kα radiation. Scanning electron microscopy (SEM) images and SEM-EDS elemental mapping were taken on a Hitachi SU8010 field emission scanning electron microscope. Transmission electron microscopy (TEM), high-resolution TEM (HRTEM) images, and STEM image and EDS elemental mappings were recorded with JEM-2010 and JEM-F200 transmission electron microscope operated at 200 kV. Atomic force microscopy (AFM) characterization was carried out on a Bruker Multimode 8 instrument under the AC mode (tapping mode). X-ray photoelectron spectra (XPS) spectra were conducted on an ESCALAB MK electron spectrometer. Specific surface areas and pore size distribution were analyzed on Micromeritics ASAP 2020 N_2 adsorption analyzer using the BET (Brunauer-Emmet-Teller) and BJH (Barrett-Joyner-Halenda) methods, respectively. Raman analysis was performed on a LabRam HR 800 laser confocal micro-Raman spectrometer (Jobin Yvon-Horiba) with a 532 nm YAG laser as the excitation source. FT-IR spectra were recorded on Bruker Tensor 27 IR spectrometer and the sample was prepared by the KBr pellet method.

2.3. Electrochemical measurements

All electrochemical measurements were carried out at room temperature on a PARSTAT 3000 electrochemical workstation using a standard three-electrode cell in 1.0 mol·L^{-1} KOH solution. Graphite rod was used as the counter electrode and Ag/AgCl (saturated KCl filled) as the reference electrode. A carbon cloth electrode with an area of 1 × 1 cm^2 used as the working electrode. Typically, 20 mg catalyst was suspended in 0.5 mL deionized water, 0.45 mL ethanol with 50 μL Nafion solution (5 wt.%, Du Pont) to form homogeneous ink assisted by ultrasound. Then 120 μL of the ink was spread onto the surface of carbon cloth by a micropipette and dried at 40 °C. The final loading for all catalysts and 20% commercial Pt/C electrocatalyst on work electrode is 2.4 mg/cm^2. The potential range was from 0 to −1.0 V (vs. Ag/AgCl) and the scan rate was 5 mV·s^{-1}. Linear sweep voltammograms (LSV) polarization curves were recorded with 90% iR-corrected. Cyclic voltammetry (CV) was carried out to calculate the capacitance (C_{dl}).

2.4. Density functional theory (DFT) calculation

The DFT calculations were conducted using the Dmol code with DN basis to express the wave function of valence electrons and DFT Semicore Pseudopots (DSPPs) to describe the interactions of valence electrons and ionic cores. The functional of generalized gradient approximation (GGA) with Perdew, Burke, and Ernzerhof (PBE) was used throughout to describe the electron–electron exchange and correlation interactions. For the sampling of Brillouin-zone integrals, a (1 × 1 × 1) k-point grid was used, and meanwhile, global Orbital cutoff 4.5 Å was

employed as the maximum value from all the cutoffs specific to each element in this system. The convergence tolerance of an energy of 10^{-5} Ha was taken, and the relaxation of the unit cell, including the atoms, was performed by Geometry Optimization. The atom positions were relaxed until the remaining force acting on the atoms was less than 4×10^{-4} Ha Å^{-1}.

The intermolecular force change (ΔE) was determined using formula, $\Delta E = E_{total} - E_{sur}$, where E_{total} is the total energy for the adsorption state and E_{sur} is the energy of pure surface. The free energy change (ΔG) for adsorptions were determined as follows: $\Delta G = E_{total} - E_{sur} + \Delta E_{ZPE} - T\Delta S$, where E_{total} is the total energy for the adsorption state, E_{sur} is the energy of pure surface, ΔE_{ZPE} is the zero-point energy change, and ΔS is the entropy change. As the vibrational entropy of H* in the adsorbed state is small, the entropy of adsorption of $1/2$ H_2 is SH $\approx$ $-0.5S_{0H2}$, where S_{0H2} is the entropy of H_2 in the gas phase at the standard conditions. Therefore, the overall corrections were taken as in $\Delta G_{H*} = E_{total} - E_{sur} - E_{H2}/2 + 0.24$ eV, where E_{H2} is the energy of H_2 in gas phase.

3. Results and discussion

3.1. formation of DESs

The formation of DESs of $NiCl_2 \cdot 6H_2O$/PEG was firstly characterized. DSC curves in Fig. S1 (see Support information) indicate that melting point (T_g) of DESs ranges from -54 to $-78\,°C$ and that DES-3 with molar ratio ($NiCl_2 \cdot 6H_2O$ to PEG) of 1:4 has the lowest T_g. In IR spectra (Fig. S2), the absorption peak at $3429\,cm^{-1}$ corresponds to the stretching of $-OH$ in PEG. After DES formation with $NiCl_2 \cdot 6H_2O$, the $-OH$ was complexed by Cl-, so the band of $-OH$ move to low wavenumber ($3350\,cm^{-1}$). This is an evidence of the formation of hydrogen bonding. It can be further confirmed from ^1H NMR spectra (Fig. S3) that after the formation of DES, the chemical shift of hydrogen in $-OH$ decreased. This is because the formation of hydrogen bond in DES between Cl^- ions and the hydrogen atom and the increase of electron cloud density of hydrogen atoms. Therefore, the polarity of the oxygen hydrogen bond is reduced, and the shielding effect is weakened.

3.2. catalysts characterization

The microstructures of the synthesized sample NiS/G-3 were characterized by using field emission scanning electron microscopy (FE-SEM) and transmission electron microscopy (TEM). Fig. 1a shows a typical SEM image of NiS/G-3 composite. The as-prepared sample possesses a 3D microsphere structure. Magnified SEM image in Fig. 1b demonstrates that the 3D microspheres were constructed with NiS/G nanosheets. Energy-dispersive X-ray spectroscopy (EDS) element mapping in Fig. 1c show homogeneously distributed Ni, S, and C elements in the as-synthesized sample. TEM image in Fig. 1d was applied to reveals the texture of an individual NiS/G nanosheet with width of about 800 nm. The observed wrinkles on the surface are curly graphene ultrathin sheets. STEM image in Fig. S5a exhibits a feature of overlapped layers of NiS and graphene ultrathin sheets. HAADF-STEM image in Fig. S5b further reveal the layered structure and the interface of the NiS and graphene layers as indicated by dashed lines. STEM-EDS elements mappings in Fig. S5c-e match the layered structure very well. HRTEM image in Fig. 1e reveals that there obviously exist plenty of boundaries in 2D NiS/G composite. Careful examination from the edge region confirms the layered structure of NiS and graphene ultrathin sheets. The continuous lattice fringes show the characteristics of NiS with the interplanar distance of 0.260 nm corresponding to (101) plane of NiS. While the curved fringes with interplanar distance of 0.370 nm correspond to the (002) planes of graphene. Further, the multi-layer structure was identified by AFM characterization. AFM image in Fig. S6a shows the multi-layered structure of the composite, while Fig. S6b shows that the sonicated sample exhibits a thin layer of nanosheet with a thickness of about 5.7 nm. In a word, design and construction of

layered 2D NiS/G heterostructure composites have been conducted via a DESs-based one-step pyrolysis accompanied sulfidation process. The unique 2D heterostructure provides possible electronic interaction between NiS and graphene and more active sites, which is essential for their enhanced catalytic activity.

XRD characterization was employed to identify the phases and crystallinity of as-prepared materials. Fig. 2a shows the corresponding XRD pattern. The main characteristic peaks at 30.0°, 34.4°, 45.5°, and 53.3° match well with (100), (101), (102) and (110) planes of hexagonal phase NiS (PDF card no. 65-5762), respectively. It agrees well with the HRTEM results. In addition, no obvious impurity peaks are assigned in XRD patterns. And the sharp and narrow characteristic peaks indicate NiS sample has high crystallinity. No obvious peaks of graphene were detected in the XRD pattern, presumably because of its relatively weak intensities compared with that of the highly crystalline NiS. So, Raman spectroscopy was carried out for further characterization. As shown in Fig. 2b, the as-prepared sample shows two typical characteristic peaks at 1354 and $1583\,cm^{-1}$, matching well with the D and G bands of graphene and corresponding to the disordered sp^2 structure and the graphene in-plane vibrations in carbon materials, respectively. Additionally, the broad and weak 2D band around $2702\,cm^{-1}$ appears suggesting the few-layered feature of the as-prepared graphene [29]. This indicates that the prepared sample is a composite of NiS and graphene. The defective and few-layered feature of the as-prepared graphene in NiS/G-3 may also contribute to the absence of observable diffraction patterns in its XRD measurements. The formation of graphene can be attributed to catalytic pyrolysis of PEG-200 in DESs media similar to that of the pyrolysis of polyhydroxy compounds [30,31]. In addition, the chemical composition of the samples was further analyzed by elemental analysis and ICP-OES, and the results are shown in Table S1. The NiS/G-3 composite has a carbon content of 10.8%.

X-ray photoelectron spectroscopy (XPS) characterization was carried to study the surface state of NiS/G-3 2D heterostructure. Fig. 2c shows the corresponding high-resolution Ni 2p spectra. The characteristic peaks at the binding energies of 853.5 and 870.8 eV can be ascribed to Ni $2p_{3/2}$ and Ni $2p_{1/2}$ of NiS [32], nevertheless, the binding energies of Ni $2p_{3/2}$ (853.0 eV) and Ni $2p_{1/2}$ (870.5 eV) of NiS/G composite exhibit a slight negative shift compared with those of pure NiS. Similarly, the binding energies for S $2p_{3/2}$ and S $2p_{1/2}$ of NiS/G also show a negative shift in comparation with those of pure NiS (Fig. 2d). The C1s spectrum in Fig. 2e can be fitted into tow peaks: the main peak at BEs of 284.7 eV is fitted to sp^2 hybridized C atoms in graphene while another peak located at 285.5 eV should be assigned to sp^2 C atoms bonded with O [33,34]. The negative shift of binding energy of Ni 2p and S 2p in NiS/G may result from the interfacial charge redistribution between NiS and graphene [35,36] suggesting the formation of coupling interaction between NiS and graphene, which would be another important factor to improve the electrocatalytic activity.

N_2 adsorption-desorption isotherm of NiS/G-3 2D heterostructure in Fig. 2f gives a distinct hysteresis loop at a relative pressure of 0.4–1.0, indicating 2D NiS/G-3 composites have type-IV isotherm with a characteristic H3 hysteresis loop. The Brunauer-Emmett-Teller (BET) surface area of NiS/G-3 2D heterostructures is $45\,m^2\,g^{-1}$. The corresponding pore size distribution plot calculated from adsorption isotherms is shown in Fig. 2f (inset). It also shows mesoporous structure and broad pore-size distribution [37]. The large specific surface area and high porosity facilitate the electrolyte penetration and transfer and can be beneficial to improve the electrocatalysis performance [38].

3.3. HER activity

The electrocatalytic activities of NiS/G-3 2D heterostructure for HER were evaluated by a three-electrode electrochemical cell in 1.0 M KOH solution. For comparison, the HER performance of NiS, graphene, and 20% Pt/C coated on carbon cloth and bare CC were also examined
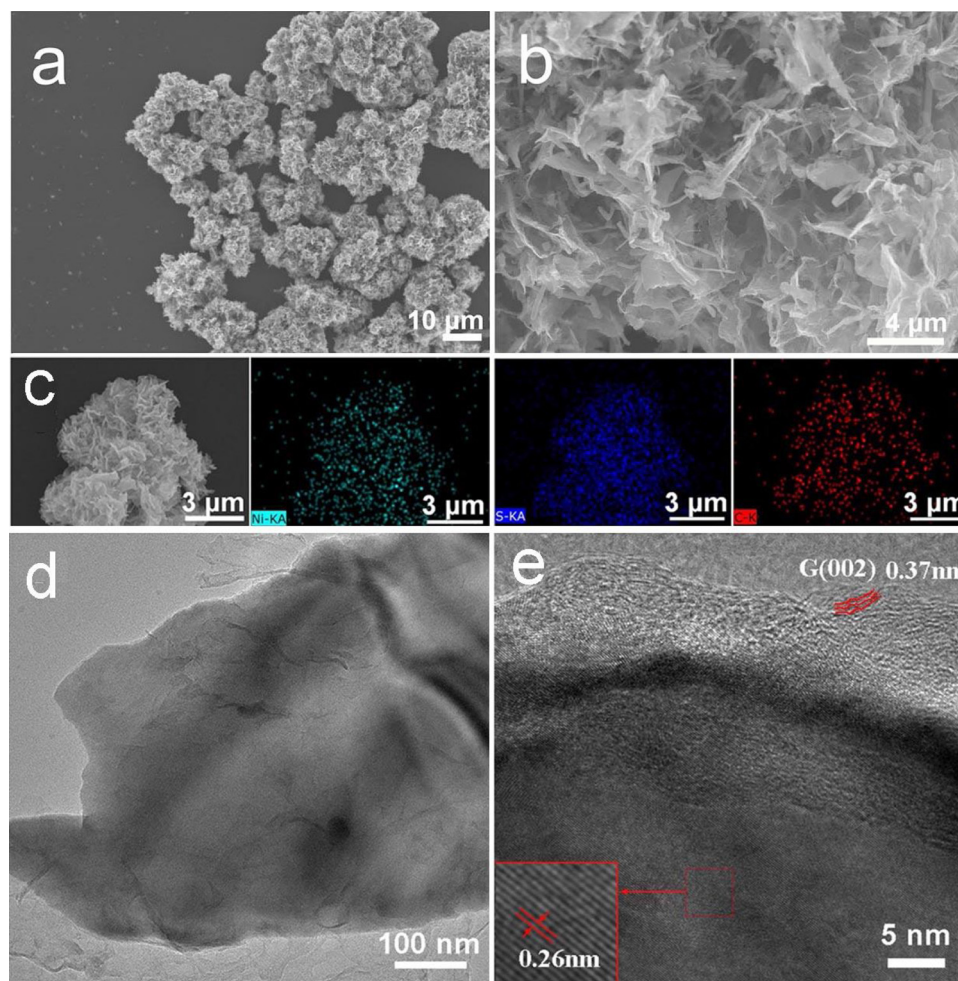
Fig. 1. SEM (a and b), EDS element mapping (c), TEM (d), and HRTEM (e) images of 2D NiS/G-3 heterostructures.
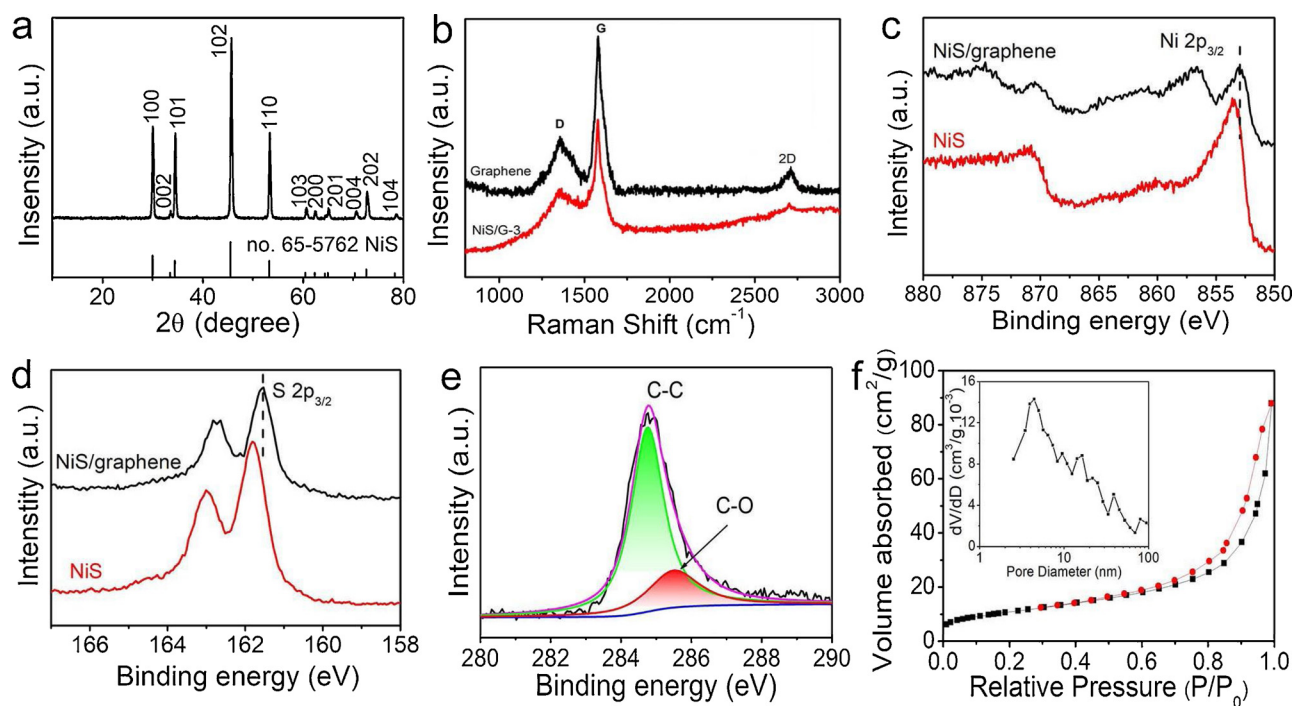

Fig. 2. (a) XRD pattern of NiS/G-3, (b) Raman spectra of NiS/G-3 and graphene, XPS spectra of (c) Ni 2p and (d) S 2p of NiS/G-3 and NiS, (e) C1s of NiS/G-3, (f) Nitrogen isotherm and pore size distribution (inset) of NiS/G-3.
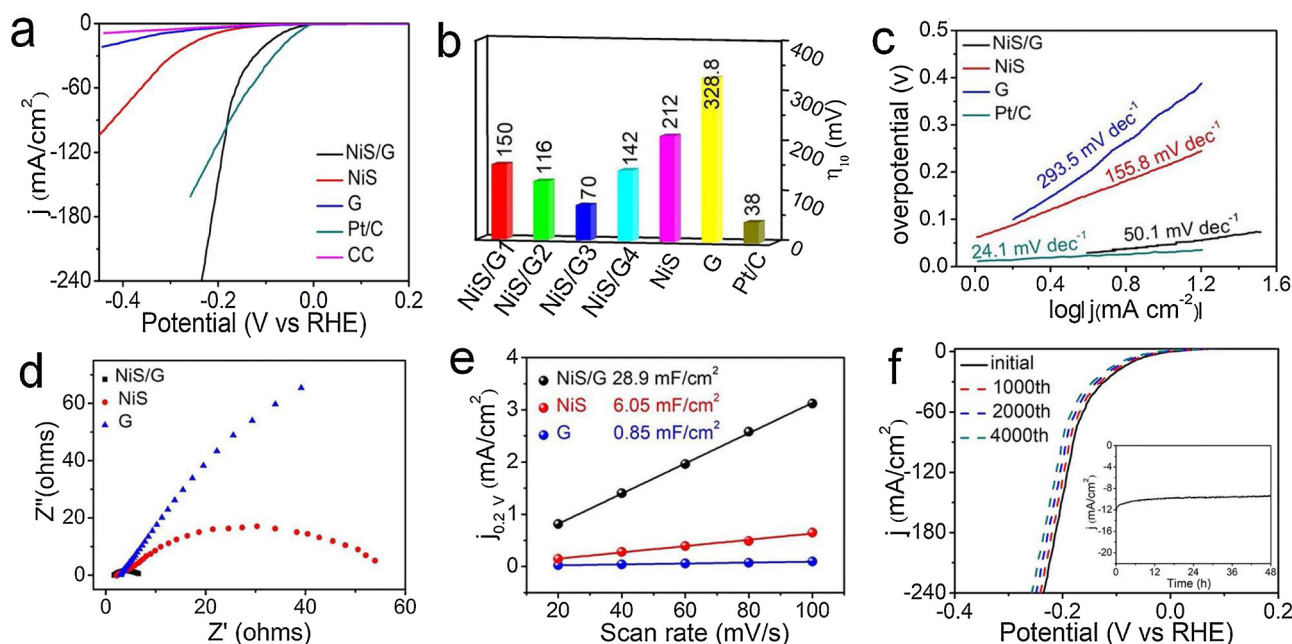
Fig. 3. (a) HER LSV curves of NiS/G, NiS, G, 20% Pt/C, and bare CC electrodes. (b) η_{10} values, (c) Tafel plots, (d) Nyquist plots (at η = 170 mV), and (e) capacitive current density versus scan rate. (f) LSV curves and time-dependent current density at 75 mV (inset) for long-term stability test of NiS/D-3.

under the same condition. Fig. 3a shows linear sweeping voltammetry (LSV) polarization curves of these electrodes. As shown in Fig. 3a, NiS/G-3 exhibits an overpotential of η_{10} = 70 mV at 10 mA cm^{-2} implying high catalytic activity for HER in alkaline solution. This η_{10} value is much lower than those of NiS (212 mV), graphene (329 mV), and carbon cloth under the same conditions, and is comparable with that of commercial 20% Pt/C (38 mV). These η_{10} values are presented in Fig. 3b for comparation. And also, NiS/G-3 catalyst exhibits super performance than 20% Pt/C at higher current density. Fig. 3c shows the corresponding Tafel plot to further evaluate the HER kinetics of these catalysts. As expected, NiS/G-3 2D heterostructure exhibits a Tafel slope of 50.1 mV·dec^{-1}, which implies that the HER process may follow a Volmer-Heyrovsky routes ($H_2O + e^- \rightarrow H_{ads} + OH^-$, $H_{ads} + H_2O + e^- \rightarrow OH^- + H_2\uparrow$) [39], in which H_{ads} represents the H atom adsorbed on the catalyst surface. Also, the Tafel slope value is much smaller than those of NiS (155.8 mV·dec^{-1}) and graphene (293.5 mV·dec^{-1}), and close to that of 20% Pt/C catalyst (24.1 mV·dec^{-1}). The lower Tafel slope indicates that NiS/G-3 2D heterostructure has a rapid HER catalytic rate in alkaline medium [40]. The obviously enhanced HER activity of 2D NiS/G heterostructure confirms the synergistic effect between NiS nanosheets and the coupled graphene ultrathin sheets. For comparison, Table S2 shows some reported HER results. It is evident that NiS/G-3 catalyst exhibits more efficient HER performance than most of the reported electrocatalysts. By extrapolating from the Tafel plots, the exchange current density of NiS/G-3 2D heterostructures is calculated to be about 1.163 mA·cm^{-2}. It is much higher than those of the currently reported NiS/Ni$_2$P (0.68 mA·cm^{-2}) [41], N doped Ni$_3$S$_2$ (0.42 mA·cm^{-2}) [42], and single-layer MoS$_2$ (0.5117 mA·cm^{-2}) [43], which indicates a higher intrinsic electron transfer rate at the interface of NiS/G-3 catalyst and electrolyte of 1.0 M KOH solution.

In addition, electrochemical impedance spectroscopy (EIS) measurements were carried out to further investigate the electrocatalytic kinetics of the catalysts and the corresponding Nyquist plots are displayed in Fig. 3d. It can be seen from Fig. 3d, the three samples showed similar solution resistance (Rs), but the charge transfer resistance (Rct) was significantly different. Similarly, NiS/G-3 2D heterostructure has a much smaller Rct than those of graphene and NiS, which indicates a superior Faradaic process and ultrafast kinetics of NiS/G-3 2D

heterostructure. The EIS results further confirm that coupling graphene with NiS nanosheets could promote the electron conductivity, contributing to the excellent HER catalytic activity. The electrochemically active surface area (ECSA) is another effective method to estimate the relative activity of electrocatalysts, which is proportional to its electrochemical double layer capacitance (Cdl) [44]. To obtain Cdl values, cyclic voltammetry (CV) curves at different scan rates were recorded and the results are presented in Fig. S7. Fig. 3e shows linear correlation of current density ($\Delta J = Ja-Jc$) of NiS/G-3, NiS and graphene plotted against scan rates at -0.2 V. The NiS/G-3 2D heterostructure has the highest C_{dl} of 28.9 m F·cm^{-2} compared with that of the NiS (6.05 m F·cm^{-2}) and graphene (0.85 m F·cm^{-2}). The calculated ECSA values for NiS/G-3, NiS, and graphene are 244.92, 51.27, and 7.20 cm^{-2}, respectively. The results demonstrating improved ECSA and greater active sites exposure by rationally designing the NiS/G-3 heterostructure nanosheets, which intrinsically enhances the catalytic activity. In addition, we calculated the turnover frequency (TOF, supporting information) of the prepared sample. At η = 300 mV, the TOF value of NiS/G-3 2D heterostructure was calculated to be 2.475 s^{-1}, which was 10.5 times as large as that of NiS (0.236 s^{-1}). The results of TOF further confirmed that constructing NiS/G-3 2D heterostructures can effectively promote HER activity. In addition to catalytic activity, NiS/G-3 2D heterostructure shows excellent long-term stability. The LSV curves before and after 4000 cycles of electrocatalysis in Fig. 3f shows just a slight increase in overpotential. Meanwhile, a stable current density of 10 mA·cm^{-2} can be maintained well at 72 mV even after 48 h of continuous operation (inset of Fig. 3f), which further confirms the high stability for HER. The SEM and XPS studies (Fig. S8) also reveal no obvious morphology and chemical state changes for the after-cycled catalyst, further suggesting the remarkable stability of the 2D NiS/G-3 catalyst. For comparation, HER performance of NiS/G prepared at different reaction conditions has also been evaluated and the results are shown in Fig. 3b and Fig. S9-11. When the pyrolysis temperature is 550 °C, the pyrolysis time is 4 h, and the precursor mole ratio is 1:4, the best HER performance of the catalyst NiS/G-3 is obtained. Decreasing or increasing PEG-200 content in the precursors leads to lower activity of the NiS/G catalysis. It proves that the synthetic condition could greatly affect the structure and HER performance of the catalysts.
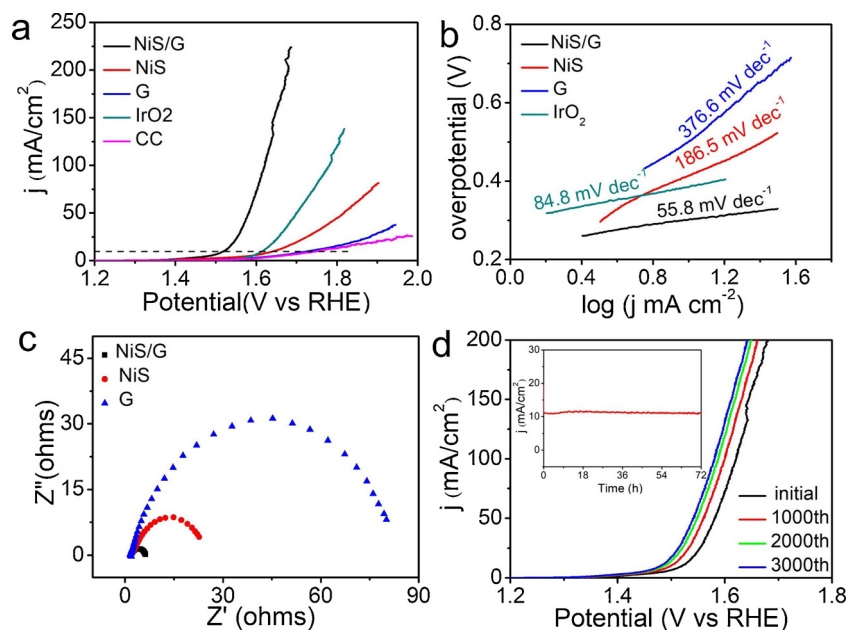
Fig. 4. (a) OER LSV curves of NiS/G, NiS, G, and IrO₂ on CC and bare CC electrodes. (b) Tafel plots and (c) Nyquist plots (at η = 300 mV) of corresponding catalysts. (d) initial and 3000 cycles of OER LSV curves and time-dependent current density at 300 mV (the inset) for long-term stability test of NiS/D-3.
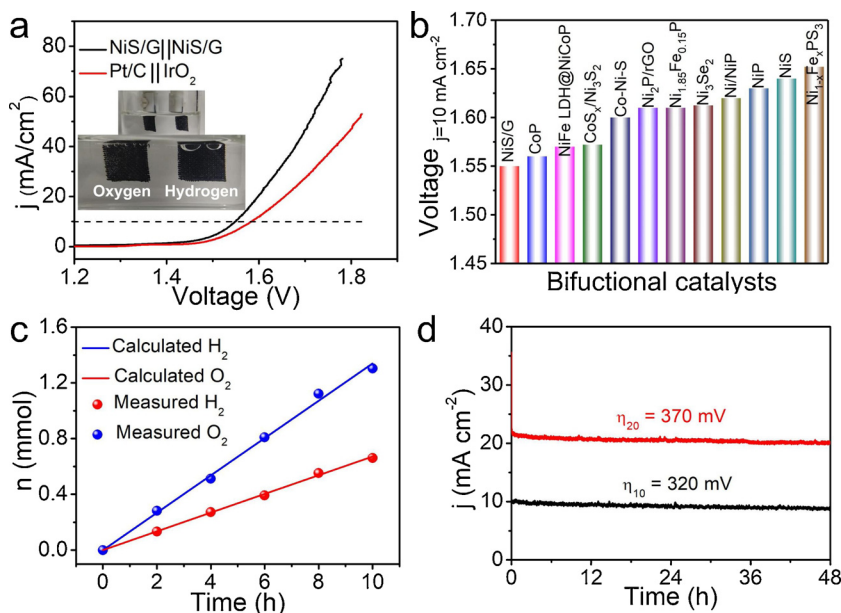

Fig. 5. (a) LSV curves of NiS/G-3 as HER and OER bifunction catalyst for overall water splitting (the inset is a digital photograph of the two-electrode cell), Pt/C and IrO₂ were measured for comparation. (b) Comparison of overpotentials between NiS/G-3 and other catalysts for overall water splitting at 10 mA·cm⁻². (c) The calculated and experimental measured H₂ and O₂ production of the NiS/G-3 at 1.55 V. (d) Long-term stability test for overall water splitting at 320 and 370 mV for 48 h, respectively.
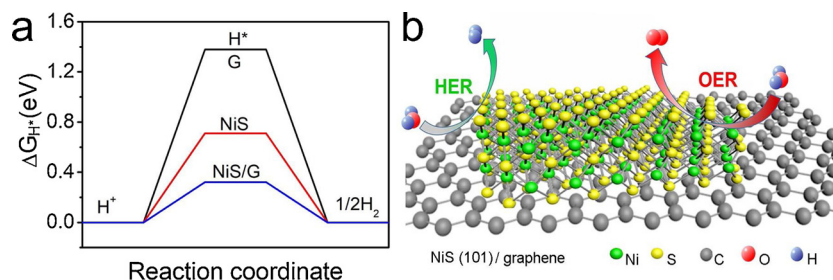

Fig. 6. (a) The ΔG_H* of different catalysts by DFT calculation. (b) Proposed overall water splitting mechanism on NiS/G.

3.4. OER activity

After studying the catalytic performance for HER, we also investigated the catalytic properties of NiS/D-3 for oxygen evolution

reaction (OER) at a scan rate of 5 mV·s⁻¹ in 1.0 mol L⁻¹ KOH solution. For comparison, the OER activity of commercial IrO₂, NiS, and G coated on CC and bare CC electrodes has also been evaluated under the same conditions. The polarization curves are present in Fig. 4a. It is identified

that NiS/G-3 2D heterostructure shows a low overpotential of 300 mV at 10 mA·cm^{-2}. The data is much lower than those of NiS and graphene, and even lower than that of IrO$_2$, which indicates that the OER catalytic efficiency has also been enhanced by coupling graphene to NiS nanosheets forming NiS/G-3 2D heterostructure. The Tafel slope of NiS/G-3 2D heterostructure was measured to be 55.8 mV·dec^{-1} (Fig. 4b), and the smallest Tafel slope value suggests its favorable OER kinetics and fast catalytic rate. The EIS results in Fig. 4c shows that NiS/G-3 2D heterostructure exhibits much smaller charge transfer resistance than those of NiS and graphene, indicating a faster charge transfer process under OER test conditions. Durability and stability are also key factors in evaluating the performance of electrocatalysts. After undergoing 3000 cycles tests, SEM image in Fig. S12a shows no obvious morphology changes confirming the structure stability of 2D NiS/G-3 catalyst. While the polarization curves in Fig. 4d shows somewhat superior OER results to the initial one, which may result from chemical state changes for the catalyst. XPS spectra in Fig. S12b indicates S2p3/2 peak almost disappears and the peak located at 168.8 eV becomes stronger, which corresponds to the surface sulfur with high oxidation state. It indicates the surface oxidation of the catalyst under the strong oxidizing environment during the OER. This phenomenon was also recently reported in the literature [45,46]. Moreover, a chronoamperometry measurement was conducted at potential 300 mA for 72 h without obvious degradation (inset of Fig. 4d), which further confirms the high OER efficiency for NiS/G-3 2D heterostructure. A comparison of the OER performance of NiS/G-3 2D heterostructure with other reported non-precious metal OER electrocatalysts is summarized in Table S3. It is clear that NiS/G-3 2D heterostructure catalyst exhibits more excellent OER performance than most of the reported OER catalysts.

3.5. Electrochemical overall water splitting

According to the above results, the NiS/G-3 2D heterostructure presents high electrocatalytic efficiency for both HER and OER. Therefore, it is expected it can serve as HER and OER bifunction catalysts for overall water splitting with a two-electrode cell in 1.0 mol L^{-1} KOH solution. The LSV results in Fig. 5a show that it requires a cell voltage of as small as 1.54 V to reach a current density of 10 mA·cm^{-2}. This efficiency for overall water splitting is higher than the benchmarks of commercial IrO$_2$ (+)//Pt/C (-) catalysts and other reported non-precious metal bifunctional catalysts (Fig. 5b) [47–57]. The calculated and experimental measured H$_2$ and O$_2$ productions at 1.55 V from overall water splitting under NiS/G-3 2D heterostructure are presented in Fig. 5c. It is evident the molar ratio of H$_2$/O$_2$ fits well in 2:1 and the total yields reach a 100% faradaic efficiency. At the same time, the NiS/G-3 2D heterostructure exhibits excellent stability after long-time testing at overpotential of 320 mV vs. RHE (Fig. 5d). When the potential increases to 370 mV, the stabilized current density correspondingly increases to 20 mA·cm^{-2} and shows no significant change within 48 h.

3.6. Electrochemical mechanism

In order to further understand the origin of the enhanced HER electrocatalytic activity of NiS/G composite, density functional theory (DFT) calculations were conducted. Fig. S13a shows the calculated H$_2$O adsorption energies on Ni, C, and S atoms of NiS/G-3 clusters. It can be seen that that H$_2$O has a largest adsorption energy on Ni atom. The strong H$_2$O-Ni bonding action implies Ni atoms act as active sites for H$_2$O adsorption. While in Fig. S13b, Gibbs free energy of hydrogen absorption (ΔG_{H*}) on C atoms is more close to zero than that of S and Ni atoms implying C atoms act as active sites for H* adsorption. It is well known that hydrogen evolution activity is related to ΔG_{H*} on the surface of the catalysts [58], which is thermodynamically required to have an appropriate value more close to zero. So, the calculated Gibbs free energies of H absorption (ΔG_{H*}) on the surfaces of catalysts of NiS/G,

NiS, and graphene is presented in Fig. 6a. As we can see from Fig. 6a, both graphene and NiS have a larger $|\Delta G_{H*}|$ value, which means H* cannot be efficiently adsorbed on their surfaces. After the two-phase recombination of graphene and NiS forming 2D NiS/G heterostructure, the ΔG_{H*} value was significantly decreased to 0.32 eV and is relatively close to the ideal ΔG_{H*} of 0 eV for the catalyst-H* state, which demonstrates that the formation of a 2D heterostructure of graphene and NiS nanosheets can really boost the HER efficiency. Thus, 2D NiS/G heterostructure exhibits the highest HER performance.

The schematic diagram in Fig. 6b illustrates the promotion effect of 2D NiS/G heterostructure improving the overall water splitting processes. Based on the above results, 2D NiS/G heterostructure serves as HER and OER bifunction catalysts for efficient overall water splitting that can be attributed to the synergistic effect of NiS layered coupling graphene. The 2D heterostructure provides unique surface/interface properties, including large specific surface area, enhanced electrical conductivity, high surface-active sites exposure, and long-time stability, which endows it with high efficiency in overall water splitting in alkaline media.

4. Conclusions

In summary, a one-step pyrolysis accompanied sulfidation method has been developed with novel DESs as precursors to construct layered 2D/2D NiS/G heterostructure composites. The designed DESs can provide a homogeneous system for sufficient contact of components, make the growing and coupling of NiS and graphene in one-step. The obtained 2D NiS/G heterostructures can serve as HER and OER catalysts with high electrocatalytic efficiency and stability in 1.0 mol L^{-1} KOH solution, and can be employed as a bifunction catalyst for overall water splitting with a cell voltage of 1.54 V at 10 mA cm^{-2}. In addition, the synthetic strategy can be extended to the preparation of other bifunctional electrocatalysts of graphene coupled non-precious-metal compound composites by carefully designing the DESs precursors.

Appendix A. Supplementary data

Supplementary material related to this article can be found, in the online version, at doi:https://doi.org/10.1016/j.apcatb.2019.05.029.

References

[1] S. Chu, Y. Cui, N. Liu, Nat. Mater. 16 (2016) 16–22.
[2] Z.W. Seh, J. Kibsgaard, C.F. Dickens, I.B. Chorkendorff, J.K. Nørskov, T.F. Jaramillo, Science 355 (2017) eaad4998.
[3] D.F. Yan, Y.X. Li, J. Huo, R. Chen, L.M. Dai, S.Y. Wang, Adv. Mater 48 (2017) 1606459.
[4] V. Artero, M. Chavarot-Kerlidou, M. Fontecave, Angew. Chem. Int. Ed. 32 (2011) 7238–7266.
[5] P.W. Du, R. Eisenberg, Energy Environ. Sci. 5 (2012) 6012–6021.
[6] R. Subbaraman, D. Tripkovic, K. Chang, D. Strmcnik, A. Paulikas, P. Hirunsit, M. Chan, J. Greeley, V. Stamenkovic, N. Markovic, Nat. Mater. 11 (2012) 550–557.
[7] S.J. Chu, W. Chen, G.L. Chen, J. Huang, R. Zhang, C.S. Song, X.Q. Wang, C.R. Li, J. (Ken) Ostrikov, Appl. Catal. B-Environ. 243 (2019) 537–545.
[8] E. Popczun, J. McKone, C. Read, A. Biacchi, A. Wiltrout, N. Lewis, R. Schaak. J. Am. Chem. Soc. 25 (2013) 9267–9270.
[9] E.J. Popczun, C.G. Read, C.W. Roske, N.S. Lewis, R.E. Schaak, Angew. Chem. Int. Ed. 53 (2014) 5427–5430.
[10] D.Y. Wang, M. Gong, H.L. Chou, C.J. Pan, H.A. Chen, Y.P. Wu, M.C. Lin, M.Y. Guan, J. Yang, C.W. Chen, Y.L. Wang, B. Hwang, C.C. Chen, H.J. Dai, J. Am. Chem. Soc. 4 (2015) 1587–1592.
[11] J. Dong, F.-Q. Zhang, Y. Yang, Y.-B. Zhang, H. He, X. Huang, X. Fan, X.-M. Zhang,

Appl. Catal. B-Environ. 243 (2019) 693–702.

[12] Y. Pei, Y.C. Ge, H. Chu, W. Smith, P. Dong, P.M. Ajayan, M.X. Ye, J.F. Shen, Appl. Catal. B-Environ. 244 (2019) 583–593.

[13] D.S. Kong, H.T. Wang, Z.Y. Lu, Y. Cui, J. Am. Chem. Soc. 136 (2014) 4897–4900.

[14] R. Boppella, J. Tan, W. Yang, J. Moon, Adv. Funct. Mater. 29 (2019) 1807976.

[15] Q.C. Xu, H. Jiang, H.X. Zhang, Y.J. Hu, C.Z. Li, Appl. Catal. B-Environ. 242 (2019) 60–66.

[16] Y. Li, J. Yin, L. An, M. Lu, K. Sun, Y.Q. Zhao, D. Gao, F.Cheng P. Xi, Small 14 (2018) 1801070.

[17] Y.G. Li, H.L. Wang, L.M. Xie, Y.Y. Liang, G.S. Hong, H.J. Dai, J. Am. Chem. Soc. 133 (2011) 7296–7299.

[18] C.S. Rout, B.H. Kim, X.D. Xu, J. Yang, H.Y. Jeong, D. Odkhuu, N. Park, J. Cho, H.S. Shin, J. Am. Chem. Soc. 23 (2013) 8720–8725.

[19] X. Yue, S.L. Huang, J.J. Cai, Y.S. Jin, P.K. Shen, J. Mater. Chem. A Mater. Energy Sustain. 5 (2017) 7784–7790.

[20] K.G. Qu, Y. Zheng, Y. Jiao, X.X. Zhang, S. Dai, S.Z. Qiao, Adv. Energy Mater. 7 (2017) 1602068.

[21] Z.H. Xue, H. Su, Q.Y. Yu, B. Zhang, H.H. Wang, X.H. Li, J.S. Chen, Adv. Energy Mater. 7 (2017) 1602355.

[22] P.Z. Chen, T.P. Zhou, M.X. Zhang, Y. Tong, C.A. Zhong, N. Zhang, L.D. Zhang, C.Z. Wu, Y. Xie, Adv. Mater. 29 (2017) 1701584.

[23] Y.Y. Wu, G.D. Li, Y.P. Liu, L. Yang, X.R. Lian, T. Asefa, X.X. Zou, Adv. Funct. Mater. 26 (2016) 4839–4847.

[24] Y.F. Cao, Y.Y. Meng, S.C. Huang, S.M. He, X.H. Li, S.F. Tong, M.M. Wu, ACS Sustain. Chem. Eng. 6 (2018) 15582–15590.

[25] C. Qu, L. Zhang, W. Meng, Z.B. Liang, B.J. Zhu, D. Dang, S.G. Dai, B.T. Zhao, H. Tabassum, S. Gao, H. Zhang, W.H. Guo, R. Zhao, X.Y. Huang, M.L. Liu, R.Q. Zou, J. Mater. Chem. A Mater. Energy Sustain. 9 (2018) 4003–4012.

[26] H.Y. Zou, B. He, P.Y. Kuang, J.G. Yu, K. Fan, Adv. Funct. Mater. 28 (2018) 1706917.

[27] E.L. Smith, A.P. Abbott, K.S. Ryder, Chem. Rev. 114 (2014) 11060–11082.

[28] Q.H. Zhang, K.De O. Vigier, S. Royera, F. Jérôme, Chem. Soc. Rev. 41 (2012) 7108–7146.

[29] C. Li, X. Zhang, K. Wang, X.Z. Sun, G.H. Liu, J.T. Li, H.F. Tian, J.Q. Li, Y.W. Ma, Adv. Mater 29 (2017) 1604690.

[30] G.D. Wen, Q.Q. Gu, Y.F. Liu, R. Schlçgl, C.X. Wang, Z.J. Tian, D. S. Su. Angew. Chem. Int. Ed. 57 (2018) 16898–16902.

[31] A. Primo, P. Atienzar, E. Sanchez, J.M. Delgado, H. García, Chem. Commun. (Camb.) 48 (2012) 9254–9256.

[32] D.L. Legrand, H.W. Nesbitt, G.M. Bancroft, Am. Mineral. 83 (1998) 1256–1265.

[33] D.C. Wei, Y.Q. Liu, Y. Wang, H.L. Zhang, L.P.Huang G. Yu, Nano Lett. 5 (2009) 1752–1758.

[34] X.S. Li, Y.W. Zhu, W.W. Cai, M. Borysiak, B.Y. Han, D. Chen, R. Piner, L. Colombo, R. Ruoff, Nano Lett. 12 (2009) 4359–4363.

[35] X.F. Liu, Z.P. Xing, H. Zhang, W. Wang, Y. Zhang, Z. Li, X. Wu, X. Yu, W. Zhou,

ChemSusChem 10 (2016) 1118–1124.

[36] B. Zhang, J. Liu, J.S. Wang, Y.J. Ruan, X. Ji, K. Xu, C. Chen, H.Z. Wan, L. Miao, Nano Energy 37 (2017) 74–80.

[37] J.L. Mohanan, I.U. Arachchige, S.L. Brock, Science 307 (2005) 397–400.

[38] W. Xing, F. Li, Z. Yan, G.Q. Lu, J. Power Sources 2 (2004) 324–330.

[39] J. Feng, H. Xu, Y. Dong, X. Lu, Y. Tong, G. Li, Angew. Chem. Int. Ed. 56 (2017) 2960.

[40] X.D. Wang, Y.F. Xu, H.S. Rao, W.J. Xu, H.Y. Chen, W.X. Zhang, D.B. Kuang, C.Y. Su, Energy Environ. Sci. 9 (2016) 1468–1475.

[41] X. Xiao, D.K. Huang, Y.Q. Fu, M. Wen, X.X. Jiang, X.W. Lv, M. Li, L. Gao, S.S. Liu, M.K. Wang, C. Zhao, Y. Shen, ACS Appl. Mater. Interfaces 10 (2018) 4689–4696.

[42] T.Y. Kou, T. Smart, B. Yao, I. Chen, D. Thota, Y. Ping, Y. Li, Adv. Energy Mater. 19 (2018) 1703538.

[43] Y. Wan, Z.Y. Zhang, X.L. Xu, Z.H. Zhang, P. Li, X. Fang, K. Zhang, K. Yuan, K.H. Liu, G.Z. Ran, Y. Li, Y. Ye, L. Dai, Nano Energy 51 (2018) 786–792.

[44] C.C.L. McCrory, S. Jung, J.C. Peters, T.F. Jaramillo, J. Am. Chem. Soc. 135 (2013) 16977–16987.

[45] H. Li, Y.D. Shao, Y.T. Su, Y.H. Gao, X.W. Wang, Chem. Mater. 28 (2016) 1155–1164.

[46] W. Chen, H.T. Wang, Y.Z. Li, Y.Y. Liu, J. Sun, S.H. Lee, J.-S. Lee, Y. Cui, ACS Cent. Sci. 1 (2015) 244–251.

[47] W. Li, X.F. Gao, D.H. Xiong, F. Xia, J. Liu, W.G. Song, J.Y. Xu, S.M. Thalluri, M.F. Cerqueira, X. Fu, L. Liu, Chem. Sci. 8 (2017) 2952–2958.

[48] H.J. Zhang, X.P. Li, A. Hähnel, V. Naumann, C. Lin, S. Azimi, S. Schweizer, A.W. Maijenburg, R.B. Wehrspohn, Adv. Funct. Mater. 14 (2018) 1706847.

[49] S. Shit, S. Chhetri, W. Jang, N.C. Murmu, H. Koo, P. Samanta, T. Kuila, ACS Appl. Mater. Interfaces 33 (2018) 27712–27722.

[50] F.F. Zhang, Y.C. Ge, H. Chu, P. Dong, R. Baines, Y. Pei, M.X. Ye, J.F. Shen, ACS Appl. Mater. Interfaces 8 (2018) 7087–7095.

[51] L.T. Yan, H.M. Jiang, Y.L. Xing, Y. Wang, D.D. Liu, X. Gu, P.C. Dai, L.J. Lia, X.B. Zhao, J. Mater. Chem. A Mater. Energy Sustain. 6 (2018) 1682–1691.

[52] P.Y. Wang, Z.H. Pu, Y.H. Li, L. Wu, Z.K. Tu, M. Jiang, Z.K. Kou, I.S. Amiinu, ACS Appl. Mater. Interfaces 31 (2017) 26001–26007.

[53] R. Xu, R. Wu, Y.M. Shi, J.F. Zhang, B. Zhang, Nano Energy 24 (2016) 103–110.

[54] G.F. Chen, T.Y. Ma, Z.Q. Liu, N. Li, Y.Z. Su, K. Davey, S.Z. Qiao, Adv. Funct. Mater. 26 (2016) 3314–3323.

[55] X.G. Wang, W. Li, D.H. Xiong, L.F. Liu, J. Mater. Chem. A Mater. Energy Sustain. 4 (2016) 5639–5646.

[56] W.X. Zhu, X.Y. Yue, W.T. Zhang, S.X. Yu, Y.H. Zhang, J.W. Wang, J.L. Wang, Chem. Commun. (Camb.) 52 (2016) 1486–1489.

[57] C.F. Du, K.N. Dinh, Q.H. Liang, Y. Zheng, Y. Luo, J.L. Zhang, Q.Y. Yan, Adv. Energy Mater. 26 (2018) 1801127.

[58] B. Hinnemann, P.G. Moses, J. Bonde, K.P. Jørgensen, J.H. Nielsen, S. Horch, I. Chorkendorff, J.K. Nørskov, J. Am. Chem. Soc. 127 (2005) 5308–5309.